

# Dynamical importance of the trade wind inversion in suppressing the southeast Pacific ITCZ

Alex Omar Gonzalez<sup>1</sup>, Indrani Ganguly<sup>2</sup>, Marissa Osterloh<sup>2</sup>, Gregory V. Cesana<sup>3</sup>, and Charlotte A Demott<sup>4</sup>

<sup>1</sup>Department of Physical Oceanography, Woods Hole Oceanographic Institution

<sup>2</sup>Department of Geological and Atmospheric Sciences, Iowa State University

<sup>3</sup>Center for Climate Systems Research, Columbia University

<sup>4</sup>Department of Atmospheric Science, Colorado State University

April 16, 2024

# Dynamical importance of the trade wind inversion in suppressing the southeast Pacific ITCZ

Alex O. Gonzalez<sup>1,2</sup>, Indrani Ganguly<sup>2</sup>, Marissa Osterloh<sup>2</sup>, Gregory V. Cesana<sup>3</sup>, and Charlotte A. DeMott<sup>4</sup>

<sup>1</sup>Department of Physical Oceanography, Woods Hole Oceanographic Institution

<sup>2</sup>Department of Geological and Atmospheric Sciences, Iowa State University

<sup>3</sup>Center for Climate Systems Research, Columbia University

<sup>4</sup>Department of Atmospheric Science, Colorado State University

## Key Points:

- East Pacific ITCZ surface wind convergence is strongly controlled by SST and boundary layer (BL) horizontal temperature gradients.
- SST gradients overemphasize the equatorial cold tongue leading to excessive equatorial divergence and latitudinally confined double ITCZs.
- BL temperature gradients show a shallow cold tongue and deep cold air below the trade wind inversion are key to maintaining a northern ITCZ.

---

Corresponding author: Alex O. Gonzalez, [alex.gonzalez@whoi.edu](mailto:alex.gonzalez@whoi.edu)

## Abstract

Sea surface temperature (SST) gradients are a primary driver of low-level wind convergence in the east Pacific Inter-Tropical Convergence Zone (ITCZ) through their hydrostatic relationship to the surface pressure gradient force (PGF). However, the surface PGF may not always align with SST gradients due to variations in boundary layer temperature gradients with height, i.e., the boundary layer contribution to the surface PGF. In this study, we investigate the observed northern hemisphere position of the east Pacific ITCZ using a slab boundary layer model (SBLM) driven by different approximations of the boundary layer virtual temperature field. SBLM simulations using the entire boundary layer virtual temperature profile produce a realistic northern hemisphere ITCZ. However, SST-only simulations produce excessive equatorial divergence and southern hemisphere convergence, resulting in a latitudinally-confined double ITCZ-like structure. Observed virtual temperature gradients highlight the importance of northward temperature gradients strengthening with height from the equator to 15 degrees south below the trade wind inversion (TWI). Our interpretation is that the equatorial cold tongue induces relatively weak high surface pressure and double ITCZ-like convergence because the resulting layer of cold air is shallow. Concurrently, relatively strong high surface pressure spreads out in the southern hemisphere due to interactions between stratocumulus clouds and the ocean surface. Together, the equatorial cold tongue and the TWI/stratocumulus clouds enable a more northern hemisphere dominant ITCZ. Thus, we provide evidence of a dynamical link between the equatorial cold tongue, low clouds, and double ITCZs, which continue to be problematic in Earth system models.

## Plain Language Summary

State-of-the-art climate models have been plagued by biases in the Inter-Tropical Convergence Zone (ITCZ), where the trade winds converge and the world's most intense rainfall occurs. Climate models often produce one ITCZ in each hemisphere, a double ITCZ, when there is nearly always one ITCZ observed in the northern hemisphere. In this study, we investigate why the northern hemisphere ITCZ dominates over the east Pacific Ocean using an idealized model driven by observed southern and northern hemisphere contrasts in: i) sea surface temperature (SST) only and ii) both SST and atmospheric temperature. Experiments driven by only SST contrasts produce a double ITCZ-like structure that is reminiscent of climate model double ITCZ biases. In observations, a cold tongue of ocean water on the equator induces relatively weak high surface pressure and a double ITCZ-like wind convergence. At the same time, relatively strong high surface pressure spreads out in the southern hemisphere due to stratocumulus clouds and the ocean surface. Together, the equatorial cold tongue and stratocumulus clouds enable a more northern hemisphere dominant ITCZ. This study provides a dynamical link between the equatorial cold tongue, low clouds, and double ITCZs, which continue to be problematic in models.

## 1 Introduction

The east Pacific Ocean intertropical convergence zone (ITCZ) is highly modulated by variations in the tropical boundary layer winds, which often produce horizontal convergence that is co-located with ITCZ precipitation (Lindzen & Nigam, 1987; Liu & Xie, 2002; Gonzalez et al., 2022). The cause of these boundary layer wind variations is commonly diagnosed through the zonal and meridional momentum budgets (Holton et al., 1971; Mahrt, 1972a, 1972b; Holton, 1975; Lindzen & Nigam, 1987; Tomas et al., 1999; McGauley et al., 2004; Raymond et al., 2006; Sobel & Neelin, 2006; Back & Bretherton, 2009a; Gonzalez & Schubert, 2019; Gonzalez et al., 2022). A leading term in boundary layer momentum budgets is the pressure gradient force (PGF), especially in regions where there are strong sea surface temperature (SST) gradients (Lindzen & Nigam, 1987; Back

& Bretherton, 2009b; Duffy et al., 2020). The link between SST and boundary layer pressure gradients comes from hydrostatic balance when integrated vertically. In a hydrostatic atmosphere, the surface pressure is determined by the density of the overlying atmospheric column. Therefore, regions with cool SSTs tend to have a higher surface pressure due to a heavier column above, and regions with warm SSTs tend to have a lower surface pressure due to a lighter column above.

Lindzen and Nigam (1987); Stevens et al. (2002); Back and Bretherton (2009a); Duffy et al. (2020), and Zhou et al. (2020) used hydrostatic balance and different forms of a linear boundary layer model to quantify how well SST gradients explain large-scale surface winds and convergence in the tropics. When integrating vertically to solve for the surface pressure gradient, most of these studies assume temperature gradients decrease with height in the boundary layer at a constant rate determined solely from the SST distribution (i.e., larger lapse rates for warm than cool SSTs). However, this assumption does not always hold true because of variations in boundary layer lapse rates that are inconsistent with SST over wide swaths of tropical latitudes. For example, near the equatorial cold tongue, SST gradients are large. However, air-sea temperature differences are minimal such that surface turbulent heat fluxes (especially sensible) are very small (Raymond et al., 2004), and the upper marine boundary layer becomes decoupled from the surface mixed layer (de Szoeke et al., 2005; Fairall et al., 2008). This implies that the layer of cool air associated with the equatorial cold tongue is shallow and should have a relatively small effect on the large-scale surface pressure gradient field. The second example is the region of cool SSTs south of the equator where there is a strong trade wind inversion (TWI) and stratocumulus clouds at the top of the boundary layer (Klein & Hartmann, 1993; Bretherton et al., 2004; Wood, 2012) surrounded by moderate SST gradients. In this region, surface turbulent heat fluxes (especially latent) are large and the boundary layer is relatively deep (Fairall et al., 2008; Kalmus et al., 2014) such that the associated cool marine boundary layer air should have a relatively large effect on the large-scale surface pressure gradient field. Additionally, the TWI layer in this region tends to be associated with strong longwave cooling at cloud top, which is a dominant term in the energy budget (Caldwell et al., 2005; Kalmus et al., 2014).

Therefore, there should be a cool anomaly associated with the TWI that is elevated and shifted southward of the near-surface cold anomaly associated with the equatorial cold tongue (Mitchell & Wallace, 1992; Mansbach & Norris, 2007). This implies that meridional temperature gradients above the surface are significantly different from SST gradients, with high surface pressure likely extending from the cold tongue to the tropical TWI and into the subtropics (Schubert et al., 1995). These ideas could help partially explain why surface winds and ITCZ convergence are more accurately diagnosed in linear boundary layer models when the surface PGF is estimated using boundary layer virtual temperature gradients (which include lapse rate variation effects) than SST gradients alone (Back & Bretherton, 2009a; Duffy et al., 2020). Furthermore, we wonder whether these ideas about localized changes in the vertical structure of boundary layer temperature gradients can help explain the overproduction of double convergence zones over the Atlantic and east Pacific in the SST-driven version of the linear boundary layer models of Back and Bretherton (2009a); Duffy et al. (2020); Zhou et al. (2020).

It is widely known that ITCZ biases in Earth system models (ESMs) can often be attributed in part to insufficient low cloud production in the southeast Pacific and/or an anomalously strong and westward extended equatorial cold tongue in the central Pacific (Mecho et al., 1995; Li & Xie, 2014; Adam et al., 2018; Woelfle et al., 2019; G. J. Zhang et al., 2019). A dearth of low clouds in ESMs is typically associated with excessive surface insolation, large atmospheric net energy input, and/or insufficient latent heat fluxes (M. H. Zhang et al., 2005; Nam et al., 2012; Cesana & Waliser, 2016; Song & Zhang, 2016; Adam et al., 2018; G. J. Zhang et al., 2019). Of all low clouds, stratocumulus clouds are of particular interest because they have cloud decks that often extend thousands of kilo-

119 meters horizontally, allowing them to potentially impact the large-scale thermodynam-  
 120 ics and dynamics. Stratocumulus clouds form at the base of a very thin ( $\mathcal{O}$  (10–100 m))  
 121 TWI layer (Haman et al., 2007; Wood, 2012) that is difficult to resolve with models (Bretherton  
 122 et al., 2004; Woelfle et al., 2019).

123 While ITCZ biases can exist in atmosphere-only model simulations (Xiang et al.,  
 124 2017, 2018), they grow substantially when ocean coupling is employed (S.-P. Xie & Phi-  
 125 lander, 1994; Lin, 2007; G. J. Zhang et al., 2019). Moreover, the significance of SST gra-  
 126 dients in driving boundary layer winds and convergence is not to be ignored. SST gra-  
 127 dients and their anomalies have been critical to understanding the interactions between  
 128 the atmosphere and ocean by anchoring the theory of wind-evaporation-SST (WES) feed-  
 129 backs, which are driven by the dynamical and surface latent heat flux response to SST  
 130 and sea level pressure anomalies (S.-P. Xie & Philander, 1994; Chelton et al., 2001; Li  
 131 & Xie, 2014). Recent work by Karnauskas (2022) demonstrated that changes in lower  
 132 atmospheric stratification, momentum mixing, and surface latent heat fluxes are also im-  
 133 portant to consider as a negative feedback mechanism that counteracts WES feedbacks  
 134 (Hayes et al., 1989; Wallace et al., 1989).

135 In this study, we seek theoretical insight into the importance of both horizontal gra-  
 136 dients of SST and boundary layer virtual temperature on surface wind convergence in  
 137 the east Pacific. We interrogate hydrostatic balance in reanalyses and develop a set of  
 138 idealized slab boundary layer model simulations with different forms of the boundary layer  
 139 contribution to the surface PGF forcing based on SST versus boundary layer virtual tem-  
 140 perature gradients. We aim to highlight the importance of changes in lapse rates, e.g.,  
 141 those associated with the TWI/low clouds, in altering the boundary layer contribution  
 142 to the surface PGF, which is known to be a driver of surface wind convergence. We deem  
 143 this the “dynamical” part, however, this is not to be confused with other important dy-  
 144 namical processes, such as the vertical mixing of horizontal momentum.

145 This paper is organized as follows. Section 2 discusses the use of atmospheric and  
 146 oceanic fields from reanalyses and low cloud fractions from the Cumulus and Stratocu-  
 147 mulus CloudSat-CALIPSO Dataset (CASCAD). We also derive two formulas, one that  
 148 decomposes the surface PGF into components from vertically integrated virtual temper-  
 149 ature gradients and free tropospheric PGF and the other to decompose virtual temper-  
 150 ature gradients into a temperature only part and a covarying moisture and temperature  
 151 part. The last part of Section 2 describes the two experiments using a nonlinear slab bound-  
 152 ary layer model (SBLM) that test different forms of the surface PGF. Section 3 begins  
 153 by comparing the meridional-vertical boundary layer virtual temperature structure be-  
 154 tween the two experiment forcings. The next parts of Section 3 analyze the surface PGF  
 155 forcings and SBLM simulation wind convergence across the two experiments. The lat-  
 156 ter parts of Section 3 tie the differences between the two SBLM simulations to localized  
 157 changes in lapse rates over the equatorial cold tongue and south of the equator (the TWI),  
 158 discussing the role of stratocumulus clouds. Section 4 summarizes the broad-reaching  
 159 results and discusses the implications within the context of a dynamical link between low  
 160 clouds, the equatorial cold tongue, and the ITCZ.

## 161 2 Methods

### 162 2.1 ERA5 Reanalysis

163 We employ various monthly atmospheric and oceanic fields from the ECMWF’s Fifth  
 164 Re-Analysis (ERA5) at a horizontal resolution of  $0.25^\circ$  for the period of 1979–2021 (Hersbach  
 165 & coauthors, 2020). A monthly climatology over 1979 to 2021 is computed for each field  
 166 of interest after which any covarying terms, numerical derivatives, or numerical integrals  
 167 are computed. Finally, all fields are zonally averaged over the east Pacific ( $90\text{--}125^\circ\text{W}$ )  
 168 using only ocean points. We use central second-order spatial finite difference methods

for both horizontal and vertical derivatives. Vertical integrals are computed using the numerical approximation presented in Table 1. We use ERA5 data because of better alignment of low cloud properties with satellite-based estimates of low clouds over the east Pacific compared to NASA’s Modern-Era Retrospective Analysis for Research and Applications, version 2 (MERRA-2, not shown). In addition, ERA5 has been shown to be more accurate than all other reanalyses in terms of vertical motions over the tropical east Pacific (Huaman et al., 2022). Serra et al. (2023) also show that ERA5 more accurately reproduces the strong tropical rainfall rates (compared to MERRA-2) observed during the Propagation of Intraseasonal Tropical Oscillations field campaign in the west Pacific.

## 2.2 The Cumulus and Stratocumulus CloudSat-CALIPSO Dataset (CASCAD)

The Cumulus and Stratocumulus CloudSat-CALIPSO Dataset (CASCAD, Cesana et al. (2019)) distinguishes stratocumulus (Sc), cumulus (Cu), and the transitioning clouds in between, i.e., broken Sc, Cu under Sc and Cu with stratiform outflow, at the orbital level based on morphology (geometrical shape and spatial heterogeneity). The CASCAD algorithm is utilized on instantaneous profiles of active-sensor CALIPSO-GOCCP (Chepfer et al., 2010) from 2007 through 2016 and CloudSat-CALIPSO GeoProf (Mace & Zhang, 2014) from 2007 through 2010. The results of a case study analysis show that CASCAD robustly captures Sc, Cu, and transitions between the two regimes, even better than previous satellite data products (Cesana et al., 2019). Thus, CASCAD represents one of the best currently-available observational constraints on the global scale distribution of Sc, which we will use in this project to study the relationship between the ITCZ, TWI, and Sc clouds over the east Pacific.

With a longer time record and a better horizontal resolution (90 m every 333 m) than CloudSat-CALIPSO GeoProf, CALIPSO-GOCCP CASCAD makes it possible to detect all fractionated shallow cumulus clouds and to analyze climatological values of Sc and Cu clouds. However, as the lidar penetrates within cloudy layers, the CALIPSO-GOCCP signal eventually attenuates completely for optical thickness greater than 3 to 5. In these instances, e.g., in deep convective clouds or in the storm tracks, the Cloud Profiling Radar (CPR) capability of CloudSat complements cloud profiles beneath the height at which the lidar attenuates, making CloudSat-CALIPSO CASCAD a better choice than CALIPSO-GOCCP CASCAD, although the CPR clutter prevents using CloudSat data below 1000 m.

## 2.3 Surface Pressure Gradient Force from Hydrostatic Balance

Given that output from ERA5 is on pressure levels, we integrate the horizontal gradient of hydrostatic balance of the form  $\frac{\partial \Phi}{\partial (\ln p)} = -R_d T_v$ , from the constant surface pressure,  $p_{sc}$ , to the top of the boundary layer,  $p_T$ , arriving at the equation

$$-\frac{1}{\rho_s} \nabla p_s = R_d \int_{p_T}^{p_{sc}} (\nabla T_v) d \ln p - (\nabla \Phi)_{p_T}. \quad (1)$$

where  $\rho_s = \rho(x, y, z_s, t)$  is the surface density,  $z_s$  is the surface height,  $p_s = p(x, y, z_s, t)$  is the surface pressure,  $\nabla$  is the horizontal gradient operator,  $T_v = \left(1 + \frac{R_v}{R_d} q\right) T$  is virtual temperature,  $R_v$  is the water vapor air gas constant,  $R_d$  is the dry air gas constant,  $T$  is temperature, and  $q$  is specific humidity. Note that the left hand side of equation (1) technically has two terms,  $-(\nabla \Phi)_{z_s}$  and  $-\frac{1}{\rho_s} \nabla p_s$ . The former term vanishes while the latter remains because we assume  $p_s$  varies with space. Equation (1) implies that the horizontal surface PGF (note the negative sign in front of  $\frac{1}{\rho_s} \nabla p_s$ ) is driven by: i) horizontal  $T_v$  gradients from the surface up until the top of the boundary layer (the boundary layer contribution) and ii) the horizontal PGF at the top of the boundary layer (here 850 hPa). Equation (1) will be numerically integrated using formulas in Table 1 for each

of two experiments using an idealized boundary layer model, which will be discussed in the next subsection.

Since the form of hydrostatic balance we use involves the role of water vapor through virtual temperature  $T_v$  rather than  $T$  alone, the role of water vapor on  $T_v$  gradients may be diagnosed by decomposing  $T_v$  gradients into two parts: one involving only  $T$  and the other involving  $q$  and  $T$ . We find that horizontal moisture gradients are typically a secondary contributor to the surface PGF over the east Pacific Ocean on the timescale of monthly climatology in this study (not shown).

## 2.4 Slab Boundary Layer Model Experiments

A zonally symmetric, slab boundary layer model (SBLM) on the sphere (Gonzalez & Schubert, 2019) is employed to simulate the surface winds of the east Pacific Ocean in a similar vein as Back and Bretherton (2009a); Duffy et al. (2020) and Zhou et al. (2020). The SBLM is forced by the boundary layer height, free tropospheric velocities (700–800 hPa averaged zonal and meridional velocity fields), and the estimated surface meridional PGF. Note that each SBLM forcing is a prescribed field from ERA5.

Consider zonally symmetric motions that depend on time  $t$  and latitude  $\phi$  of an incompressible fluid of a frictional boundary layer of variable depth  $h$ . The boundary layer zonal and meridional velocities  $u(\phi, t)$  and  $v(\phi, t)$  are independent of height between the top of a thin surface layer and height,  $h$ , and the vertical velocity at the top of the boundary layer is denoted by  $w(\phi, t)$ . The governing system of differential equations is

$$\frac{\partial u}{\partial t} + v \frac{\partial u}{a \partial \phi} = f_e v - c_D U \frac{u}{h} + \frac{w^-}{h} (u - u_{\text{FT}}) + K_u, \quad (2)$$

$$\frac{\partial v}{\partial t} + v \frac{\partial v}{a \partial \phi} = -f_e u - c_D U \frac{v}{h} - \frac{1}{\rho_s} \frac{\partial p_s}{\partial y} + \frac{w^-}{h} (v - v_{\text{FT}}) + K_v, \quad (3)$$

$$w = -\frac{\partial(hv \cos \phi)}{a \cos \phi \partial \phi}, \quad (4)$$

where  $f_e = \left(2\Omega \sin \phi + \frac{u \tan \phi}{a}\right)$  is the effective Coriolis force, including the metric term,  $\Omega$  and  $a$  are Earth's rotation rate and radius,  $c_D U$  is the parameterized surface wind drag factor (more details below),  $U = 0.78 (u^2 + v^2)^{1/2}$  is the wind speed at 10 meter height (Powell et al., 2003),  $w^- = \frac{1}{2} (|w| - w)$  is the rectified Ekman suction,  $u_{\text{FT}}(\phi)$  and  $v_{\text{FT}}(\phi)$  are the respective zonal and meridional velocities in the overlying free troposphere,  $K_u = K \frac{\partial}{a \partial \phi} \left( \frac{\partial(hu \cos \phi)}{a \cos \phi \partial \phi} \right)$  is the zonal diffusion,  $K_v = K \frac{\partial}{a \partial \phi} \left( \frac{\partial(hv \cos \phi)}{a \cos \phi \partial \phi} \right)$  is the meridional diffusion, and  $K$  is the constant horizontal diffusivity. The drag factor  $c_D U$  is assumed to depend on the 10 meter wind speed according to the following formula from (Large et al., 1994)

$$c_D U = 10^{-3} (2.70 + 0.142U + 0.0764U^2). \quad (5)$$

A derivation of the SBLM equations starting from first conservation principles is given in the Appendix of Gonzalez and Schubert (2019). For all experiments, the constants used are  $\Omega = 7.292 \times 10^{-5} \text{ s}^{-1}$ ,  $a = 6.371 \times 10^6 \text{ m}$ ,  $K = 1.0 \times 10^6 \text{ m}^2 \text{ s}^{-1}$ ,  $\Delta t = 300 \text{ s}$ , and  $\Delta \phi = 0.25^\circ$ .

We perform a suite of SBLM simulations, one for each month of the year and over two different experiments for a total of 24 simulations (see Table 1). Each of the two SBLM experiments contains the same prescribed boundary layer height,  $h$ , free tropospheric velocities,  $u_{\text{FT}}$ ,  $v_{\text{FT}}$ , and 850 hPa PGF,  $\left(\frac{\partial \Phi}{\partial y}\right)_p$ , but they have a different form of the boundary layer contribution to the surface PGF forcing,  $R_d \int_{p_T}^{p_{sc}} \frac{\partial T_v}{\partial y} d \ln p$ : i) surface to 850 hPa, mass-weighted and vertically-integrated  $T_v$  gradients (Full  $T_v$ ) and ii) SST gradients (SST-only), which is described below. We also performed two additional experiments that are



shown in the supplemental information, Figures S2 and S3: iii)  $T_v$  gradients averaged over 850–900 hPa ( $T_{v,850-900}$ ) and iv) 850 hPa PGF ( $\text{PGF}_{850}$ ).

For all experiments, horizontal gradients are computed before selecting ocean-only points and before computing pressure level averages. Given that the Full  $T_v$  SBLM experiments involve numerical integration, we quantify the month-by-month errors in the Full  $T_v$  surface PGF against the “observed” surface PGF in Figure S1. The observed surface PGF is estimated using second-order central finite difference methods via the equation,

$$-\frac{1}{\rho_s} \nabla p_s = -R_d (\text{SST}) \nabla \ln p_s, \quad (6)$$

where SST is the sea surface temperature. We find that the numerically integrated Full  $T_v$  surface PGF is quite accurate, with a minimum pattern correlation of 0.999 and a maximum standardized root-mean-squared difference of 0.066 compared to the estimate from equation (6). Note since the SBLM is a zonally symmetric model, only the meridional component ( $\partial/\partial y$ ) of the surface PGF is used in this study. However, the use of the  $\nabla$  gradient operator is retained to keep the derivations as general as possible for future applications.

For the SST-only SBLM experiment, the assumption is that  $T_v$  gradients linearly decay with pressure (Lindzen & Nigam, 1987; Duffy et al., 2020; Zhou et al., 2020) according to the formula

$$\nabla T_v(p) = \nabla \text{SST} \left( 1 - \delta_T \frac{(p_{sc} - p)}{(p_{sc} - p_T)} \right), \quad (7)$$

where  $\delta_T$  is a fraction representing how fast the SST gradient linearly decays from the surface to the top of the boundary layer. For this study, we choose  $\delta_T = 0.75$ , which implies that the SST gradients have decayed by 75% at  $p = p_T$ . The assumption of the SST gradient only changing in magnitude in the vertical allows for the surface PGF forcing formula in (1) to be written as

$$-\frac{1}{\rho_s} \nabla p_s = R_d \ln \left( \frac{p_{sc}}{p_T} \right) A \nabla \text{SST} - (\nabla \Phi)_{p_T}, \quad (8)$$

where

$$A = 1 - \delta_T \left( \frac{p_{sc}}{p_{sc} - p_T} - \frac{1}{\ln(p_{sc}/p_T)} \right). \quad (9)$$

Using the constant values  $p_{sc} = 1013$  hPa,  $p_T = 850$  hPa, and  $\delta_T = 0.75$ ,  $A = 0.614$ , which implies that the net amplitude (when vertically integrated) of the SST gradient on the surface PGF is 61.4% due to the assumption of the SST gradient decaying linearly with height.

Note that for the entirety of the paper, SBLM simulation solutions will be shown at the equilibrium time of 30 days, which is when the meridional integral of the kinetic energy tendency vanishes over the entire domain (not shown). For comparisons between the dynamical solutions of the SBLM versus boundary layer (850–1000 hPa) averaged ERA5 data, see Figures S2 and S3 in the Supporting Information section.

### 3 Results

#### 3.1 Variation of Virtual Temperature Gradients within the Boundary Layer

We begin by comparing and contrasting the vertical structure of the observed meridional  $T_v$  gradients with those of the SST-only  $T_v$  from equation (7) during the contrasting months of September and March using ERA5 data.



**Table 1.** The two SBLM experiments, including the numerical equations used to estimate the surface PGF forcings. We use  $p_T = 850$  hPa for both experiments and  $p_s = 1013$  hPa for the SST-only experiment. For Full  $T_v$ , the SST is used in place of  $T_v$  at the surface and the surface pressure is the observed mean sea level pressure,  $i$  corresponds to each pressure level from the surface to 850 hPa, and  $N$  is the total number of pressure and surface levels (e.g., eight in ERA5).

Experiment	Surface PGF Equation
Full $T_v$	$R_d \sum_{i=1}^{N-1} (\nabla T_{v_i}) \ln \left( \frac{p_{i+1}}{p_i} \right) - (\nabla \Phi)_{p_T}$
SST-only	$R_d A (\nabla \text{SST}) \ln \left( \frac{p_{sc}}{p_T} \right) - (\nabla \Phi)_{p_T}$

For September, Figure 1a,c shows that observed and SST-only  $T_v$  gradients broadly agree that there are northward  $T_v$  gradients everywhere except from 5–10°S to the equator which is associated with the atmospheric signature of the equatorial cold tongue seen in Figure 1b,d. Figure 1e shows that most of the differences occur in the upper boundary layer, as expected, but the largest differences are present throughout the boundary layer near the equator. There is a strong northward  $T_v$  gradient anomaly near the equator in SST-only because the equatorial cold tongue signal is stronger and it is also shifted slightly south. Upper boundary layer  $T_v$  gradient anomalies highlight that there are consistently stronger observed southward  $T_v$  gradients in SST-only above the surface. Furthermore, there is a significant change in the observed  $T_v$  gradient with height within the boundary layer that is not readily seen in SST-only. For example, there is a complete reversal in the observed  $T_v$  gradient with height over 6°S–EQ, which we hypothesize will play a role in mitigating strong equatorial divergence in SST-only SBLM simulations. In addition, Figure 1a shows that there is a northward tilt in the observed northward  $T_v$  gradient with height near 5°N that is not present in SST-only. Most of the differences in observed and SST-only  $T_v$  gradients are due to temperature gradient effects with moisture gradient effects acting to increase northward  $T_v$  gradients, especially south of the ITCZ and in the upper boundary layer (not shown).

Since it may be difficult to conceptualize  $T_v$  gradients, Figure 1b,d,f shows the vertical structure of the observed anomalous  $T_v$ , SST-only  $T_v$ , and SST-only minus  $T_v$  for September. Note that the anomalous SST-only  $T_v$  is recovered through latitudinal integration of equation (7) and removal of the 20°S–20°N mean  $T_v(p)$  profile. The observed and SST-only  $T_v$  anomalies for September show broad warm  $T_v$  in the northern hemisphere (NH) and cool  $T_v$  in the southern hemisphere (SH). The equatorial cold tongue signature is weaker in the observed  $T_v$  anomaly compared to the SST-only  $T_v$  anomaly. However, the SST-only cold tongue anomaly is of a similar magnitude as the SST-only cold and warm  $T_v$  anomalies away from the equator, the observed  $T_v$  cold tongue anomaly is about one third as strong as of the observed cool and warm  $T_v$  anomalies away from the equator.

Figure 2a,c shows that observed and SST-only  $T_v$  gradients are generally weaker during March than September. As seen in Figure 2e, differences between these  $T_v$  gradients are largest in the upper boundary layer south of 5°S but they are otherwise quite weak. Similar to September, the atmospheric signal of the equatorial cold tongue is stronger and deeper in the SST-only  $T_v$  gradients compared to observed  $T_v$  gradients. Most of the differences in observed and SST-only  $T_v$  gradients are due to temperature gradient effects, however, moisture gradient effects do play a relatively larger role in March compared to September (not shown). This is not surprising based on our crude scale anal-

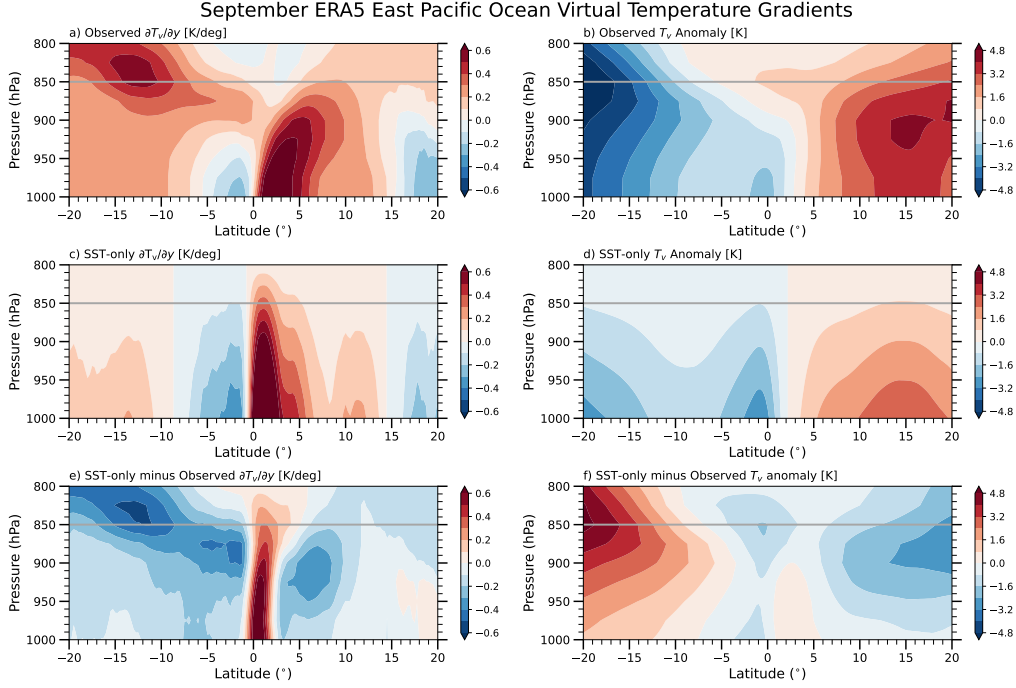


**Figure 1.** ERA5 meridional  $T_v$  gradients and  $T_v$  anomalies averaged over the east Pacific Ocean (90-125°W) during September: a) observed  $\partial T_v / \partial y$ , b) observed  $T_v$  anomaly, c) SST-only  $\partial T_v / \partial y$ , d) SST-only  $T_v$  anomaly, e) SST-only minus observed  $\partial T_v / \partial y$ , and f) SST-only minus observed  $T_v$  anomaly.  $T_v$  anomalies are relative to the 20°S–20°N mean.

333 ysis in section 2.3, as we expected moisture gradient effects to be most significant dur-  
 334 ing months when temperature gradients are smallest.

335 The observed and SST-only  $T_v$  anomalies for March in Figure 2b,d show broad sim-  
 336 ilarities with those of September with relatively warm  $T_v$  north of the equator and a cool  
 337 anomaly (elevated in observed  $T_v$ ) south of 10°S. Furthermore, SST-only  $T_v$  anomalies  
 338 show an equatorial cold tongue signature that is nearly absent from the observed  $T_v$  ana-  
 339 lies. However, the differences between the observed and SST-only  $T_v$  anomalies are sub-  
 340 stantially smaller in March compared to September (note the reduced contour levels in  
 341 Figure 2f).

### 342 3.2 Surface PGF SBLM Forcings

343 To help with our interpretations of how the differences in boundary layer merid-  
 344 ional  $T_v$  gradients impact the SBLM surface PGF forcing fields for each of our SBLM  
 345 experiments, Figure 3a,b shows the “surface geopotential anomaly” during September  
 346 and March using ERA5 data. The surface geopotential anomaly is technically the lat-  
 347 itudinally integrated surface PGF field from Figure 3c,d with the 20°S–20°N mean re-  
 348 moved. We examine the surface PGF (and its surface geopotential anomaly) because it  
 349 is our only varying forcing between our SBLM experiments and it is one of the three lead-  
 350 ing terms in the meridional momentum budget in all of our SBLM simulations, as shown  
 351 in Figure S6.

352 The surface geopotential anomalies associated with both surface PGF SBLM forc-  
 353 ings show broadly that September is dominated by high geopotential south of the equa-

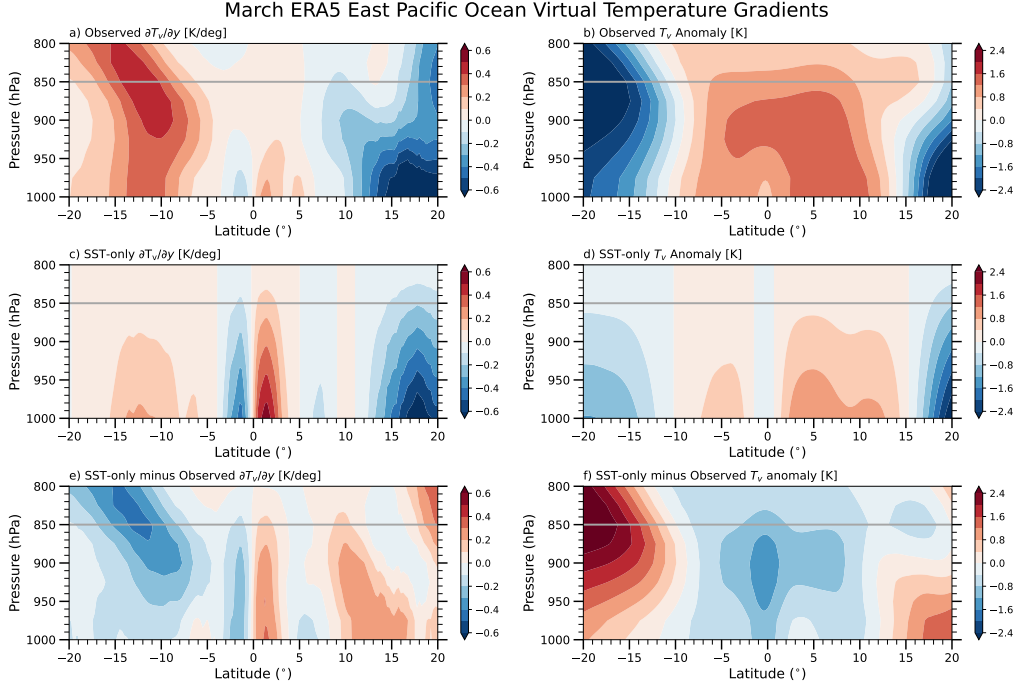


**Figure 2.** Same as Figure 1 but for March.

tor and low geopotential north of the equator (Figure 3a). From this general latitudinal structure of geopotential, one would expect a northern ITCZ to develop in all SBLM simulations. During March, both surface PGF forcings also show qualitative agreement that surface geopotential anomalies are nearly symmetric about the equator with low geopotential anomalies centered about the equator (Figure 3b). Thus, one would expect either one single ITCZ centered on the equator or two ITCZs straddling the equator, i.e., a double ITCZ, during March. A double ITCZ structure typically occurs when there is a relatively high geopotential centered on the equator (Figure 3b) or the surface PGF switches from negative to positive abruptly near the equator (Figure 3d), inducing divergence away from the equator (Gonzalez et al., 2016). Thus, we anticipate a double ITCZ to be produced from the SST-only and Full  $T_v$  (to a lesser extent) SBLM simulations during March (Figure 3b,d,f, blue curves). Despite many broad similarities between both surface PGF forcings, there are key differences between the SBLM surface PGF forcings for Full  $T_v$  (black) and SST-only (blue).

South of  $5^\circ\text{S}$  during both September and March, the high surface geopotential anomalies and positive PGF are consistently weaker in SST-only (Figure 3a–d, blue curves) than in Full  $T_v$  (black curves). This would suggest that SST-only SBLM simulations have an anomalous low south of the equator and not enough SH divergence and/or too much SH convergence. Near the equator during September and March, SST-only surface geopotential anomalies are anomalously higher than in Full  $T_v$  (Figure 3a,b), implying there may be excessive equatorial divergence and a double ITCZ structure in SST-only SBLM simulations. SST-only surface geopotential anomalies are generally anomalously higher than in Full  $T_v$  north of  $3^\circ\text{N}$  during September and from  $3^\circ\text{N}$ – $12^\circ\text{N}$  during March. Given that the ITCZ is located near  $5^\circ\text{N}$ – $15^\circ\text{N}$  in September and  $3^\circ\text{N}$ – $8^\circ\text{N}$  in March (Liu & Xie, 2002), one would expect these anomalously high surface geopotential anomalies to yield weaker NH ITCZ convergence in SST-only than in Full  $T_v$  SBLM simulations.

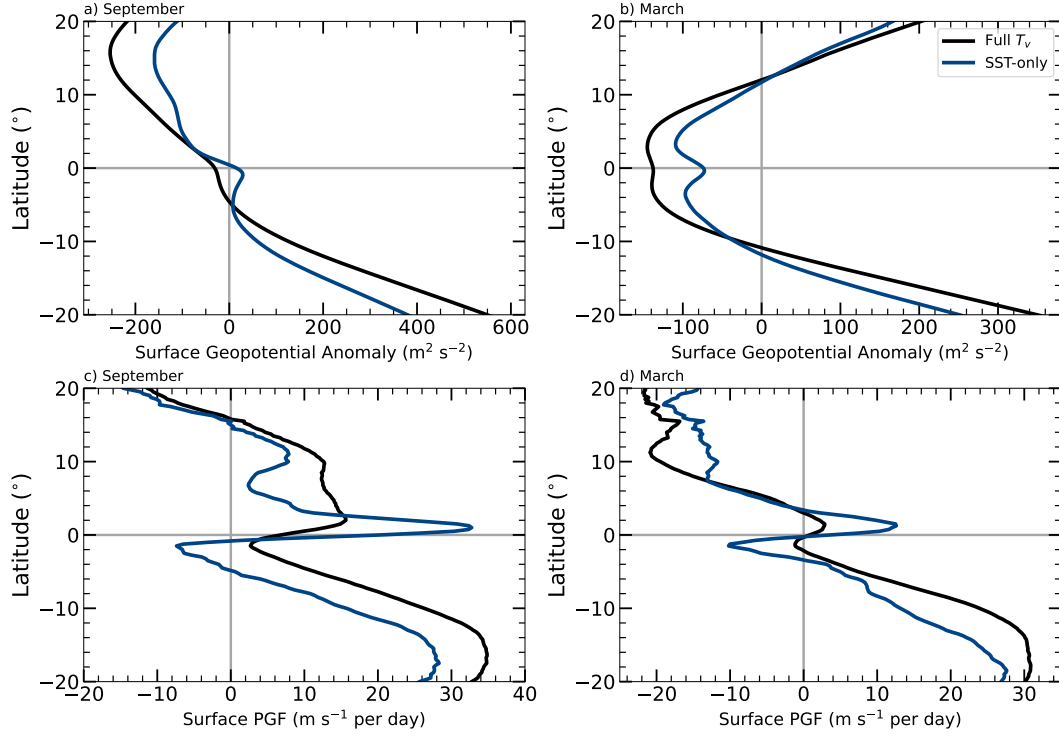


**Figure 3.** ERA5 surface geopotential anomalies and pressure gradient force (PGF) averaged over the east Pacific Ocean (90–125°W) for the two SBLM experiments (see Table 1): Full  $T_v$  (black) and SST-only (blue) during the months of a,c) September and b,d) March. Note that geopotential anomalies are calculated via latitudinal integration of equations (1) or (8) and they are relative to the 20°S–20°N mean.

### 3.3 Surface Wind Convergence from the SBLM Experiments

Figure 4b,c illustrates that SST-only SBLM simulations produce a year-round double ITCZ and excessive equatorial divergence compared to Full  $T_v$  SBLM simulations. In observations and reanalyses, a double ITCZ peaks during February through April (C. Zhang, 2001; Liu & Xie, 2002; Gu et al., 2005; Gonzalez et al., 2022). Surface wind convergence in SST-only SBLM simulations is much more interhemispherically symmetric especially during May through December despite there being a robust NH ITCZ in both wind convergence and precipitation observations (Waliser & Gautier, 1993). Furthermore, the NH ITCZ in SST-only SBLM simulations is consistently shifted south of the NH ITCZ in Full  $T_v$ . These findings confirm our hypotheses when we analyzed the  $T_v$  and surface PGFs that the observed north-south asymmetries in boundary layer  $T_v$  (e.g., Figure 1) are critical in the production a NH-dominant ITCZ in observations.

From Figure 4, it is evident that SST-only SBLM simulations overproduce equatorial divergence and southern hemisphere convergence and have a more equatorward NH ITCZ. However, how significant the off-equatorial convergence and equatorial divergence pattern biases are in SST-only SBLM simulations relative to Full  $T_v$  SBLM simulations is not as clear. This is relevant since SH convergence is present all year in the Full  $T_v$  SBLM simulations and in observations (Liu & Xie, 2002; Gonzalez et al., 2022) but it is relatively weak for most of the year in observations, especially compared to NH convergence. Figure 5a suggests there is indeed a substantial pattern problem in SST-only SBLM simulations in that SH convergence is from two times to an order of magnitude too strong compared to NH convergence for all months except from February through April. Furthermore, Figure 5b shows that SST-only SBLM simulations have excessive SH convergence compared to equatorial (EQ) divergence (one and a half to an order of magnitude too strong) during July through December. February through April also show substantial discrepancies in SST-only SBLM simulations, with EQ divergence being three to five times too strong compared to SH convergence. Overall, we center the rest of our analyses on the idea that SH convergence is too strong compared to EQ divergence and NH convergence in SST-only SBLM simulations during the months of June through December, peaking in September.

### 3.4 Connection to the TWI and Low Clouds

To better quantify the reasons for the seasonal change in the vertical structure of equatorial and southern hemisphere meridional  $T_v$  gradients, Figure 6a,b shows the disappearance of the TWI from September to March in ERA5. Associated with the TWI during September is a clear difference in the vertical structure of  $T_v$  at both 7.5°S and the EQ compared to the 30°S–30°N domain mean profile (Figure 6c). Both locations experience relative warming above cooling during September, with the cool anomaly at 7.5°S centered well above the surface at 900 hPa and the maximum cooling at the EQ near the surface. Figure 6d shows that during March, it is relatively warm throughout the vertical profile of  $T_v$  at both locations, with a significant increase in lapse rate above 925 hPa. This increase in lapse rate in the upper boundary layer and lower free troposphere during March is likely related to the weakening of the equatorial cold tongue and the development of convection in and near the SH ITCZ.

Coming back to the connection between the TWI and changing meridional  $T_v$  gradients with height discussed in Figures 1 and 2, Figure 6e computes the difference between the 7.5°S and EQ  $T_v$  profiles for both September and March. The differences in vertical  $T_v$  structure between 7.5°S and the EQ suggest there is an increased north-south  $T_v$  gradient in the upper part of the boundary layer (cooler to the south) and a decreased temperature gradient near the surface (cooler at the EQ) during both September and March. It is the displacement of these two cool anomalies that causes the differences in

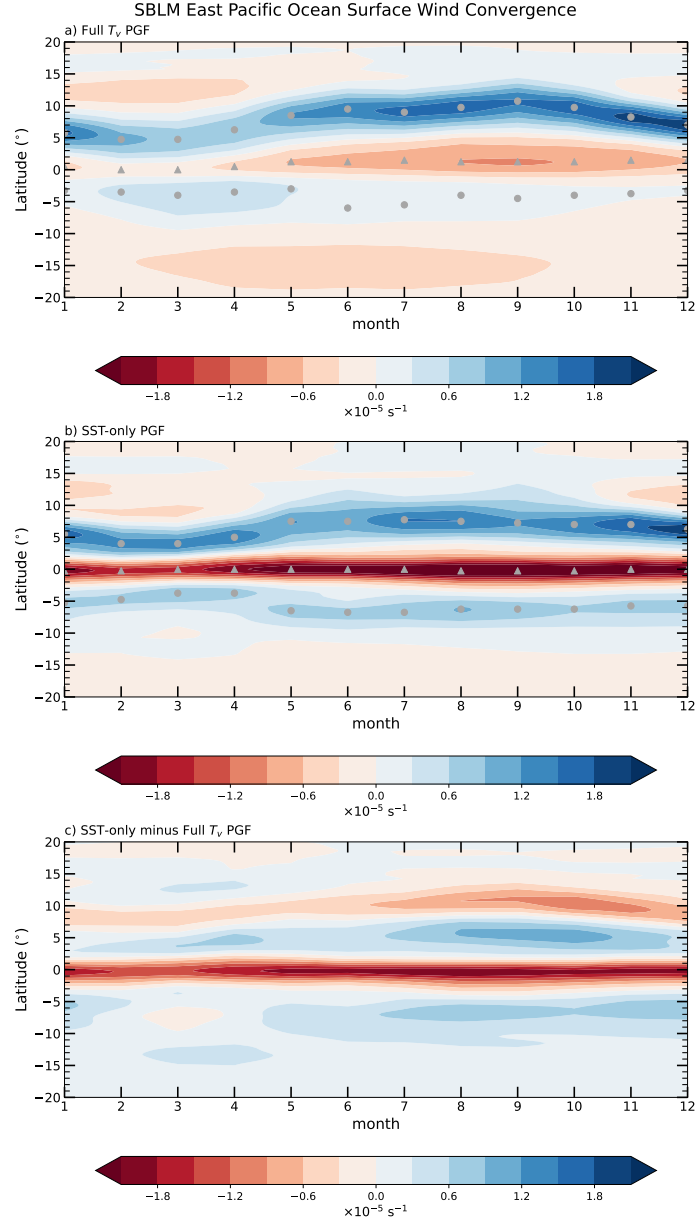


**Figure 4.** SBLM-simulated surface wind convergence over the east Pacific Ocean (90-125°W) for the two experiments: a) Full  $T_v$  PGF and b) SST-only PGF. Panel c shows SST-only minus Full  $T_v$  PGF surface wind convergence. In panels a and b, the gray circles are the latitudes of maximum SH and NH convergence and the gray triangles are the latitudes of maximum equatorial divergence.

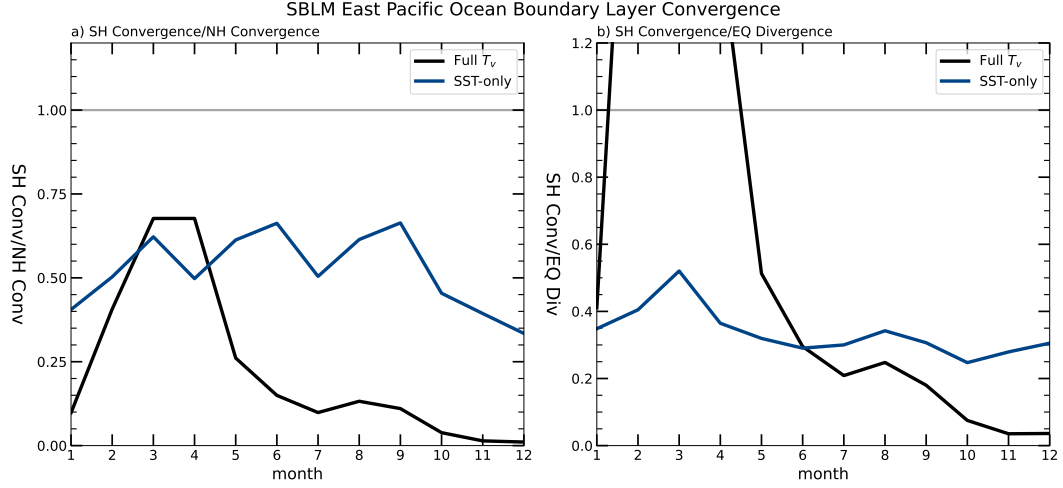


**Figure 5.** The ratios of the: a) maxima of NH convergence and SH convergence and b) maxima of equatorial divergence and SH convergence for the Full  $T_v$  PGF (black) and SST-only PGF (blue) SBLM simulations. The SH and NH convergence maxima correspond to the convergence in the gray circles Figure 4a,b. The equatorial divergence maxima correspond to the divergence in gray triangles of Figure 4a,b.

the resulting boundary layer contribution to the surface PGF and convergence between Full  $T_v$  and SST-only SBLM simulations (Figures 3 and 4).

Reincorporating the ideas formulated with respect to Figure 3, the SST cold tongue signature at the equator causes a high surface pressure and a prominent equatorially confined double ITCZ structure. In the upper boundary layer, the cool anomaly is displaced south of the equator, which contributes to a displacement of the high surface pressure south of the equator and a relaxation of the double ITCZ structure. These effects are due to the localized (at the equator and in the SH) changes in lapse rates in the 800–900 hPa layer, which are tied to the presence of the TWI and low-level cloud decks (namely, stratocumulus clouds).

Figure 7 shows the stratocumulus (Sc) cloud fraction in a) CloudSat-CALIPSO and b) GOCCP CASCAD at 7.5°S (shaded) and EQ (black contour lines) as a function of month of the year and averaged over the east Pacific (90–125°W). As expected, the Sc cloud fraction maximizes just below the 850 hPa level (1.2 km) from August through October similarly to TWI layer lapse rates minimizing during September in ERA5. Sc cloud fraction minimizes during February through April, which also agrees with the maxima in TWI layer lapse rates during March in ERA5. Despite the slightly different magnitude of Sc cloud fraction between the Cloudsat-CALIPSO CASCAD and GOCCP CASCAD, the two datasets show general agreement in monthly evolution, especially at 7.5°S. One noticeable difference is that Cloudsat-CALIPSO CASCAD shows a peak in Sc cloud fraction at the EQ that is slightly lower in altitude (700 m–1 km) compared to GOCCP CASCAD ( $\approx 1.2$  km). This shallower Sc feature is reminiscent of the equatorial TWI being located lower in height (875–900 hPa) than the 7.5°S TWI (850 hPa) in Figure 6a,b. A latitudinal cross-section during September supports the presence of this tilt of Sc low clouds with latitude, as shown in Figure S7. Despite a slightly smaller Sc fraction and a slight deviation in the height of maximum Sc fraction, GOCCP CASCAD manages to capture Sc cloud fractions to the same extent as CloudSat-CALIPSO. This is even true during March when convection could attenuate the low cloud signal based on sub-



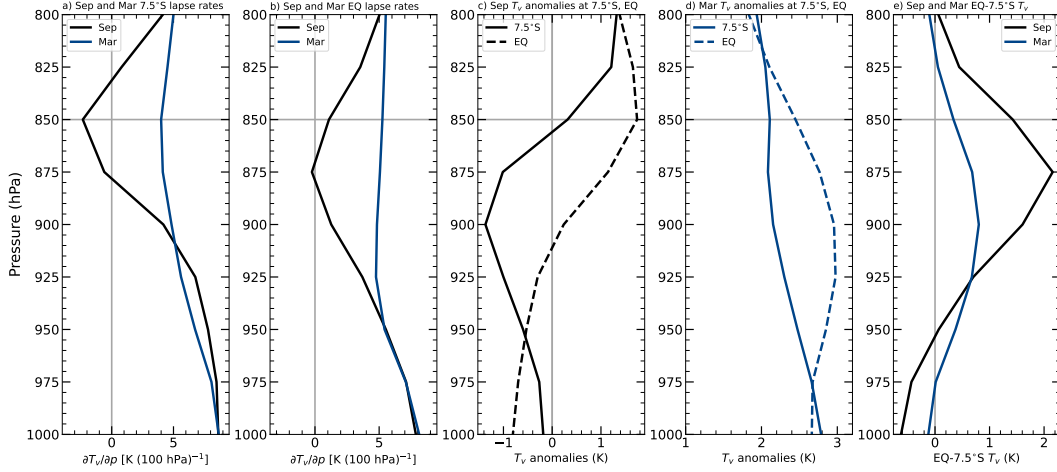


**Figure 6.** ERA5  $\partial T_v/\partial p$  over the east Pacific Ocean (90-125°W) at a) 7.5°S and b) EQ for September (black) and March (blue).  $T_v$  anomaly (relative to the 30°S–30°N mean  $T_v$ ) at 7.5°S (solid) and EQ (dashed) for c) September (black) and d) March (blue). e) EQ minus 7.5°S  $T_v$  for September (black) and March (blue), which highlights the change in direction of the  $T_v$  gradient near 950–975 hPa.

sequent analyses of the vertical profiles of ERA5 specific humidity and vertical pressure velocity (not shown).

## 4 Summary and Conclusions

In this study, we have illustrated the important role of meridional virtual temperature ( $T_v$ ) gradients varying with height in the boundary layer on ITCZ wind convergence over the east Pacific Ocean on monthly timescales. We employed an idealized, slab boundary layer model to conduct two main experiments using different boundary layer contributions to the surface pressure gradient force (PGF) prescribed from ERA5 reanalysis data: i) mass-weighted, boundary layer (surface–850 hPa) integrated  $T_v$  PGF (Full  $T_v$ ) and ii) SST-only PGF.

We find that two factors distinguish near-surface meridional  $T_v$  gradients from those in the upper boundary layer. Near the surface, the equatorial cold tongue’s atmospheric signature promotes strong equatorial divergence and off-equatorial convergence, promoting a double ITCZ-like structure. In the upper boundary layer, a northern ITCZ is preferred due to a cool anomaly that is shifted 15 to 20 degrees south of the equator that is associated with a strong trade wind inversion (TWI) above it and a high fraction of stratocumulus low clouds slightly below it. Another interpretation, based on hydrostatic balance as a relationship between surface pressure and density of the atmosphere above, is that the ITCZ is less prevalent near the equator and south of the equator because the atmospheric column (mainly the boundary layer) is denser (cooler and drier) than it is north of the equator due to the elevated cool anomaly in the SH and the equatorial cold tongue. These main ideas are conceptualized in Figure 8, which shows the ERA5  $T_v$  averaged over the east Pacific Ocean and relative to the 30°S–30°N mean.

Our SBLM experiments show that the largest discrepancies in ITCZ wind convergence between the SST-only and Full  $T_v$  SBLM simulations occur at the same time that the equatorial cold tongue, the TWI, and stratocumulus clouds peak in intensity during June through December. Our interpretation is that the cool SSTs in the SH trop-

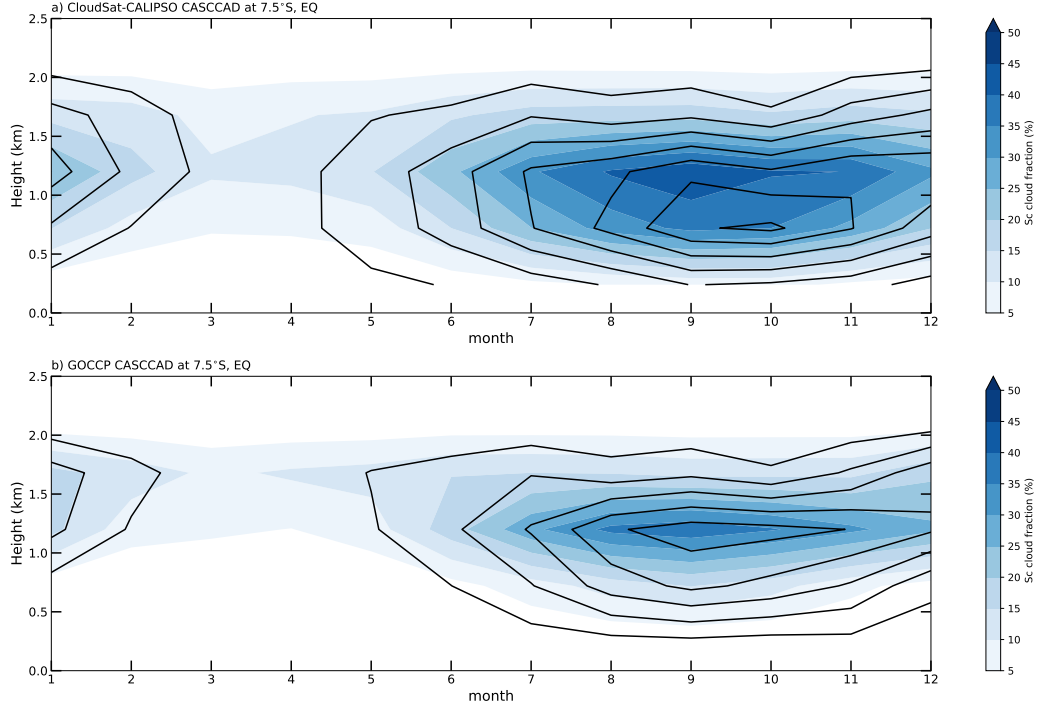


**Figure 7.** Stratocumulus (Sc) cloud fraction (%) averaged over the east Pacific Ocean (90–125°W) at 7.5°S (shaded) and EQ (black contour lines) as a function month and height for a) Cloudsat-CALIPSO CASCAD (2007–2010) and b) GOCCP CASCAD (2007–2016).

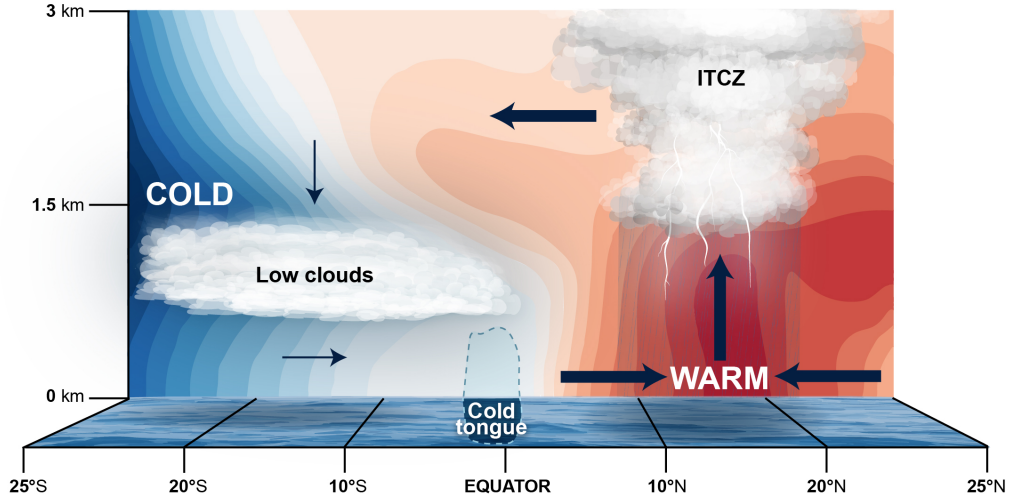


**Figure 8.** Conceptual figure of the importance of the cooling: i) at the top of Sc low clouds and ii) near the equatorial cold tongue on ITCZ wind convergence. (Contours) The ERA5  $T_v$  anomaly (relative to the 30°S–30°N mean  $T_v$ ) averaged over the east Pacific Ocean (90–125°W) during September.

ics are generally unfavorable for ITCZ convection but together with strong surface latent heat fluxes and subsidence from the the Hadley circulation, they promote the development of the TWI and stratocumulus clouds. These stratocumulus clouds subsequently block insolation which further cools down the sea surface and promotes a positive feedback loop (Myers et al., 2018). This positive feedback is likely further reinforced by the strong longwave radiative cooling at the top of stratocumulus clouds, which has been shown to dominate their energy budget (Caldwell et al., 2005; Kalmus et al., 2014). This cooling extends throughout the boundary layer and helps provide a large-scale north-to-south (NH versus SH) asymmetry in ITCZ convergence and mitigates the excessively strong equatorial divergence and SH ITCZ convergence that would otherwise be produced by the SST distribution alone. At the same time, the equatorial cold tongue is associated with less equatorial divergence and double ITCZ convergence than the SST distribution would suggest. The reasons for this cannot be confirmed with our idealized model but based on observations it is likely that the SSTs reach a lower threshold that makes it difficult to turbulently mix the air vertically (Raymond et al., 2004), decoupling the surface layer from the rest of the boundary layer (de Szoeke et al., 2005; Fairall et al., 2008).

While SST gradients can help explain essential features of the east Pacific ITCZ, such as the year-round weak convergence in the SH (Liu & Xie, 2002) and more latitudinally concentrated ITCZ convection (Gonzalez et al., 2016), this study is a cautionary reminder that  $T_v$  gradients well above the surface (but still within the boundary layer) altered by the interactions between low clouds and the underlying ocean also play a key role in the observed preference of a NH-dominant ITCZ in the east Pacific Ocean (Mitchell & Wallace, 1992; Mechoso et al., 1995; Philander et al., 1996; Nigam, 1997; Takahashi & Battisti, 2007; Woelfle et al., 2019). The relatively straight-forward comparison of SST-only versus boundary layer  $T_v$  gradients on surface wind convergence could help shed light on sources of double ITCZ biases in models. While coupled models may suffer more from double ITCZ biases than atmosphere-only models, models with prescribed SSTs can still have significant issues with low-level stratocumulus clouds (Lin, 2007; Xiang et al., 2017, 2018; Woelfle et al., 2019; G. J. Zhang et al., 2019). We plan to extend our methods to understand not only modeled climatological ITCZ variability but also subseasonal (Haffke et al., 2016; Gonzalez et al., 2022) and interannual variability (R. Xie & Yang, 2014; Yang & Magnusdottir, 2016; S.-P. Xie et al., 2018).

Our interpretations broadly agree with ideas formulated about latitudinal ITCZ shifts by the energy balance framework (Schneider et al., 2014; Kang et al., 2018). That is, double ITCZs are favored when there is a dearth of equatorial atmospheric net energy input (i.e., the cold tongue is too strong, Bischoff and Schneider (2014, 2016); Adam et al. (2016); Schneider (2017)) and/or there is too much atmospheric net energy input in the southern hemisphere (i.e., there is a lack of low clouds, Hwang and Frierson (2013); Adam et al. (2016, 2018)). We describe our findings within the framework of a “dynamical” link between the TWI/low clouds, the equatorial cold tongue, and the ITCZ mainly because we scrutinize the ITCZ based on surface wind convergence. However, as implied by our analyses of the vertical structure of virtual temperature, our ideas connect to thermodynamic and energy-based frameworks. There is much more to be learned about these connections, such as low- to mid-free tropospheric moisture, moist static energy, and turbulent mixing fit into the big picture of what controls tropical winds and convection in and near the ITCZ (Holloway & Neelin, 2009; Stevens et al., 2017; Yu & Pritchard, 2019; Fuchs-Stone et al., 2020; Raymond & Fuchs-Stone, 2021; Stevens & Coauthors, 2021).

## Open Research Section

The ERA5 reanalysis data on pressure levels can be found in ECMWF (2023). The CASCAD data can be downloaded from Cesana (2019). All output from each of the SBLM experiments can be found in Gonzalez (2024). All scripts used to produce each figure in this paper is in Gonzalez (2023).

## Acknowledgments

We would like to acknowledge stimulating conversations with Kristopher Karnauskas and Richard Neale throughout the course of this project. AOG and IG were supported by NSF AGS-1953944 and AGS-2303225. MO was supported by Iowa State University’s Dean’s High Impact Undergraduate Research Award and NSF AGS-1953944. CAD was supported by NSF OCE 1924659.

## References

- Adam, O., Bischoff, T., & Schneider, T. (2016). Seasonal and interannual variations of the energy flux equator and ITCZ. Part I: Zonally averaged ITCZ position. *J. Climate*, *29*(9), 3219–3230. doi: 10.1175/JCLI-D-15-0512.1
- Adam, O., Schneider, T., & Brient, F. (2018). Regional and seasonal variations of the double-ITCZ bias in CMIP5 models. *Climate Dyn.*, *51*, 101–117. doi: 10.1007/s00382-017-3909-1
- Back, L. E., & Bretherton, C. S. (2009a). On the relationship between SST gradients, boundary layer winds and convergence over the tropical oceans. *J. Climate*, *22*, 4182–4196. doi: 10.1175/2009JCLI2392.1
- Back, L. E., & Bretherton, C. S. (2009b). A simple model of climatological rainfall and vertical motion patterns over the tropical oceans. *J. Climate*, *22*(23), 6477–6497. Retrieved from <https://doi.org/10.1175/2009JCLI2393.1> doi: 10.1175/2009JCLI2393.1
- Bischoff, T., & Schneider, T. (2014). Energetic constraints on the position of the intertropical convergence zone. *J. Climate*, *27*(13), 4937–4951. doi: 10.1175/JCLI-D-13-00650.1
- Bischoff, T., & Schneider, T. (2016). The equatorial energy balance, ITCZ position, and double-ITCZ bifurcations. *J. Climate*, *29*(8), 2997–3013. doi: 10.1175/JCLI-D-15-0328.1
- Bretherton, C. S., Uttal, T., Fairall, C. W., Yuter, S. E., Weller, R. A., Baumgardner, D., ... Raga, G. B. (2004). The epic 2001 stratocumulus study. *Bulletin of the American Meteorological Society*, *85*(7), 967 - 978. Retrieved from <https://journals.ametsoc.org/view/journals/bams/85/7/bams-85-7-967.xml> doi: 10.1175/BAMS-85-7-967
- Caldwell, P., Bretherton, C. S., & Wood, R. (2005). Mixed-layer budget analysis of the diurnal cycle of entrainment in southeast pacific stratocumulus. *Journal of the Atmospheric Sciences*, *62*(10), 3775 - 3791. Retrieved from <https://journals.ametsoc.org/view/journals/atsc/62/10/jas3561.1.xml> doi: <https://doi.org/10.1175/JAS3561.1>
- Cesana, G. (2019). *The cumulus and stratocumulus cloudsat-calipso dataset (cascad)*. [Dataset]. Retrieved from <https://data.giss.nasa.gov/clouds/casccad/>
- Cesana, G., Del Genio, A. D., & Chepfer, H. (2019). The cumulus and stratocumulus cloudsat-calipso dataset (casccad). *Earth System Science Data*, *11*(4), 1745–1764. Retrieved from <https://essd.copernicus.org/articles/11/1745/2019/> doi: 10.5194/essd-11-1745-2019
- Cesana, G., & Waliser, D. E. (2016). Characterizing and understanding systematic biases in the vertical structure of clouds in cmip5/cfmip2 models. *Geophysical Research Letters*, *43*(19), 10,538-10,546. Retrieved from <https://agupubs.onlinelibrary.wiley.com/doi/abs/10.1002/2016GL070515> doi: <https://doi.org/10.1002/2016GL070515>
- Chelton, D. B., Esbensen, S. K., Schlax, M. G., Thum, N., Freilich, M. H., Wentz, F. J., ... Schopf, P. S. (2001). Observations of coupling between surface wind stress and sea surface temperature in the eastern tropical pacific. *Journal of Climate*, *14*(7), 1479 - 1498. Retrieved from [https://journals.ametsoc.org/view/journals/clim/14/7/1520-0442.2001.014.1479\\_oocbsw.2.0.co.2](https://journals.ametsoc.org/view/journals/clim/14/7/1520-0442.2001.014.1479_oocbsw.2.0.co.2)

- .xml doi: 10.1175/1520-0442(2001)014(1479:OOCBSW)2.0.CO;2
- Chepfer, H., Bony, S., Winker, D., Cesana, G., Dufresne, J. L., Minnis, P., ... Zeng, S. (2010). The gcm-oriented calipso cloud product (calipso-goccp). *Journal of Geophysical Research: Atmospheres*, 115(D4). Retrieved from <https://agupubs.onlinelibrary.wiley.com/doi/abs/10.1029/2009JD012251> doi: <https://doi.org/10.1029/2009JD012251>
- de Szoeke, S. P., Bretherton, C. S., Bond, N. A., Cronin, M. F., & Morley, B. M. (2005). Epic 95°w observations of the eastern pacific atmospheric boundary layer from the cold tongue to the itcz. *Journal of the Atmospheric Sciences*, 62(2), 426 - 442. Retrieved from <https://journals.ametsoc.org/view/journals/atasc/62/2/jas-3381.1.xml> doi: <https://doi.org/10.1175/JAS-3381.1>
- Duffy, M. L., O’Gorman, P. A., & Back, L. E. (2020). Importance of laplacian of low-level warming for the response of precipitation to climate change over tropical oceans. *Journal of Climate*, 33(10), 4403 - 4417. Retrieved from <https://journals.ametsoc.org/view/journals/clim/33/10/jcli-d-19-0365.1.xml> doi: 10.1175/JCLI-D-19-0365.1
- ECMWF. (2023). *Era5 monthly averaged data on single levels from 1940 to present*. [Dataset]. Retrieved from <https://cds.climate.copernicus.eu/cdsapp#!/dataset/reanalysis-era5-pressure-levels>
- Fairall, C. W., Uttal, T., Hazen, D., Hare, J., Cronin, M. F., Bond, N., & Veron, D. E. (2008). Observations of cloud, radiation, and surface forcing in the equatorial eastern pacific. *Journal of Climate*, 21(4), 655 - 673. Retrieved from <https://journals.ametsoc.org/view/journals/clim/21/4/2007jcli1757.1.xml> doi: <https://doi.org/10.1175/2007JCLI1757.1>
- Fuchs-Stone, v., Raymond, D. J., & Sentić, S. (2020). Otrec2019: Convection over the east pacific and southwest caribbean. *Geophysical Research Letters*, 47(11), e2020GL087564. Retrieved from <https://agupubs.onlinelibrary.wiley.com/doi/abs/10.1029/2020GL087564> (e2020GL087564 2020GL087564) doi: <https://doi.org/10.1029/2020GL087564>
- Gonzalez, A. O. (2023). *Dynamical importance of the trade wind inversion in suppressing the southeast pacific itcz*. [Software]. Retrieved from [https://github.com/agon1985/ITCZ\\_lowclouds](https://github.com/agon1985/ITCZ_lowclouds)
- Gonzalez, A. O. (2024). *Slab boundary layer model simulations for “Dynamical importance of the trade wind inversion in suppressing the southeast Pacific ITCZ”*. [Dataset]. Retrieved from <https://doi.org/10.26025/1912/67493>
- Gonzalez, A. O., Ganguly, I., McGraw, M. C., & Larson, J. G. (2022). Rapid dynamical evolution of itcz events over the east pacific. *Journal of Climate*, 35(4), 1197 - 1213. Retrieved from <https://journals.ametsoc.org/view/journals/clim/35/4/JCLI-D-21-0216.1.xml> doi: 10.1175/JCLI-D-21-0216.1
- Gonzalez, A. O., & Schubert, W. H. (2019). Violation of Ekman balance in the eastern Pacific ITCZ boundary layer. *J. Atmos. Sci.*, 76(9), 2919–2940. doi: 10.1175/JAS-D-18-0291.1
- Gonzalez, A. O., Slocum, C. J., Taft, R. K., & Schubert, W. H. (2016). Dynamics of the ITCZ boundary layer. *J. Atmos. Sci.*, 73(4), 1577–1592. doi: 10.1175/JAS-D-15-0298.1
- Gu, G., Adler, R. F., & Sobel, A. H. (2005). The eastern Pacific ITCZ during the boreal spring. *J. Atmos. Sci.*, 62, 1157–1174.
- Haffke, C., Magnusdottir, G., Henke, D., Smyth, P., & Peings, Y. (2016). Daily states of the March–April east Pacific ITCZ in three decades of high-resolution satellite data. *J. Climate*, 29(8), 2981–2995. doi: 10.1175/JCLI-D-15-0224.1
- Haman, K. E., Malinowski, S. P., Kurowski, M. J., Gerber, H., & Brenguier, J.-L. (2007). Small scale mixing processes at the top of a marine stratocumulus—a case study. *Quarterly Journal of the Royal Meteorological Society*, 133(622),



- 213-226. Retrieved from <https://rmets.onlinelibrary.wiley.com/doi/abs/10.1002/qj.5> doi: <https://doi.org/10.1002/qj.5>
- Hayes, S. P., McPhaden, M. J., & Wallace, J. M. (1989). The influence of sea surface temperature on surface wind in the eastern equatorial Pacific: Weekly to monthly variability. *J. Climate*, *2*, 1500–1506.
- Hersbach, H., & coauthors. (2020). The ERA5 global reanalysis. *Quart. J. Roy. Meteor. Soc.*, *146*(730), 1999–2049. doi: [10.1002/qj.3803](https://doi.org/10.1002/qj.3803)
- Holloway, C. E., & Neelin, J. D. (2009). Moisture vertical structure, column water vapor, and tropical deep convection. *Journal of the Atmospheric Sciences*, *66*(6), 1665–1683. Retrieved from <https://journals.ametsoc.org/view/journals/atsc/66/6/2008jas2806.1.xml> doi: [10.1175/2008JAS2806.1](https://doi.org/10.1175/2008JAS2806.1)
- Holton, J. R. (1975). On the influence of boundary layer friction on mixed Rossby-gravity waves. *Tellus*, *27*, 107–115. doi: [10.1111/j.2153-3490.1975.tb01664.x](https://doi.org/10.1111/j.2153-3490.1975.tb01664.x)
- Holton, J. R., Wallace, J. M., & Young, J. A. (1971). On boundary layer dynamics and the ITCZ. *J. Atmos. Sci.*, *28*, 275–280. doi: [10.1175/1520-0469\(1971\)028<0275:OBLDAT>2.0.CO;2](https://doi.org/10.1175/1520-0469(1971)028<0275:OBLDAT>2.0.CO;2)
- Huaman, L., Schumacher, C., & Sobel, A. H. (2022). Assessing the vertical velocity of the east pacific itcz. *Geophysical Research Letters*, *49*(1), e2021GL096192. Retrieved from <https://agupubs.onlinelibrary.wiley.com/doi/abs/10.1029/2021GL096192> (e2021GL096192 2021GL096192) doi: <https://doi.org/10.1029/2021GL096192>
- Hwang, Y.-T., & Frierson, D. M. W. (2013). Link between the double-intertropical convergence zone problem and cloud biases over the Southern Ocean. *Proc. Natl. Acad. Sci. (USA)*, *110*(13), 4935–4940. doi: [10.1073/pnas.1213302110](https://doi.org/10.1073/pnas.1213302110)
- Kalmus, P., Lebsock, M., & Teixeira, J. (2014). Observational boundary layer energy and water budgets of the stratocumulus-to-cumulus transition. *Journal of Climate*, *27*(24), 9155–9170. Retrieved from <https://journals.ametsoc.org/view/journals/clim/27/24/jcli-d-14-00242.1.xml> doi: <https://doi.org/10.1175/JCLI-D-14-00242.1>
- Kang, S. M., Shin, Y., & Xie, S.-P. (2018). Extratropical forcing and tropical rainfall distribution: energetics framework and ocean Ekman advection. *npj Climate and Atmospheric Science*, *1*(20172). doi: [10.1038/s41612-017-0004-6](https://doi.org/10.1038/s41612-017-0004-6)
- Karnauskas, K. B. (2022). A simple coupled model of the wind–evaporation–sst feedback with a role for stability. *Journal of Climate*, *35*(7), 2149–2160. Retrieved from <https://journals.ametsoc.org/view/journals/clim/35/7/JCLI-D-20-0895.1.xml> doi: [10.1175/JCLI-D-20-0895.1](https://doi.org/10.1175/JCLI-D-20-0895.1)
- Klein, S. A., & Hartmann, D. L. (1993). The seasonal cycle of low stratiform clouds. *Journal of Climate*, *6*(8), 1587–1606. Retrieved from [https://journals.ametsoc.org/view/journals/clim/6/8/1520-0442\\_1993.006.1587\\_tscols.2.0\\_co.2.xml](https://journals.ametsoc.org/view/journals/clim/6/8/1520-0442_1993.006.1587_tscols.2.0_co.2.xml) doi: [10.1175/1520-0442\(1993\)006<1587:TSCOLS>2.0.CO;2](https://doi.org/10.1175/1520-0442(1993)006<1587:TSCOLS>2.0.CO;2)
- Large, W. G., McWilliams, J. C., & Doney, S. C. (1994). Oceanic vertical mixing: A review and a model with a nonlocal boundary layer parameterization. *Rev. Geophys.*, *32*(4), 363–403. doi: [10.1029/94RG01872](https://doi.org/10.1029/94RG01872)
- Li, G., & Xie, S.-P. (2014). Tropical Biases in CMIP5 Multimodel Ensemble: The Excessive Equatorial Pacific Cold Tongue and Double ITCZ Problems. *J. Climate*, *27*(4), 1765–1780. doi: [10.1175/JCLI-D-13-00337.1](https://doi.org/10.1175/JCLI-D-13-00337.1)
- Lin, J.-L. (2007). The double-ITCZ problem in IPCC AR4 coupled GCMs: Ocean–atmosphere feedback analysis. *J. Climate*, *20*(18), 4497–4525. doi: [10.1175/JCLI4272.1](https://doi.org/10.1175/JCLI4272.1)
- Lindzen, R. S., & Nigam, S. (1987). On the role of sea surface temperature gradients in forcing low-level winds and convergence in the tropics. *J. Atmos. Sci.*, *44*, 2418–2436. doi: [10.1175/1520-0469\(1987\)044<2418:OTROSS>2.0.CO;2](https://doi.org/10.1175/1520-0469(1987)044<2418:OTROSS>2.0.CO;2)
- Liu, W. T., & Xie, X. (2002). Double intertropical convergence zones—A new look using scatterometer. *Geophys. Res. Lett.*, *29*, 2092.

- Mace, G. G., & Zhang, Q. (2014). The cloudsat radar-lidar geometrical profile product (rl-geoprof): Updates, improvements, and selected results. *Journal of Geophysical Research: Atmospheres*, 119(15), 9441-9462. Retrieved from <https://agupubs.onlinelibrary.wiley.com/doi/abs/10.1002/2013JD021374> doi: <https://doi.org/10.1002/2013JD021374>
- Mahrt, L. J. (1972a). A numerical study of the influence of advective accelerations in an idealized, low-latitude, planetary boundary layer. *J. Atmos. Sci.*, 29, 1477-1484. doi: 10.1175/1520-0469(1972)029<1477:ANSOTI>2.0.CO;2
- Mahrt, L. J. (1972b). A numerical study of the influence of advective accelerations in an idealized, low-latitude, planetary boundary layer2. *J. Atmos. Sci.*, 29, 1477-1484. doi: 10.1175/1520-0469(1972)029<1477:ANSOTI>2.0.CO;2
- Mansbach, D. K., & Norris, J. R. (2007). Low-level cloud variability over the equatorial cold tongue in observations and models. *Journal of Climate*, 20(8), 1555 - 1570. Retrieved from <https://journals.ametsoc.org/view/journals/clim/20/8/jcli4073.1.xml> doi: <https://doi.org/10.1175/JCLI4073.1>
- McGauley, M., Zhang, C., & Bond, N. (2004). Large-scale characteristics of the atmospheric boundary layer in the eastern Pacific cold tongue-ITCZ region. *J. Climate*, 17, 3907-3920. doi: 10.1175/1520-0442(2004)017<3907:LCOTAB>2.0.CO;2
- Mechoso, C., Robertson, A., Barth, N., Davey, M., Delecluse, P., Gent, P., ... Tribbia, J. (1995). The seasonal cycle over the tropical Pacific in coupled ocean-atmosphere general circulation models. *Mon. Wea. Rev.*, 123(9), 2825-2838. doi: 10.1175/1520-0493(1995)123<2825:TSCOTT>2.0.CO;2
- Mitchell, T. P., & Wallace, J. M. (1992). The annual cycle in equatorial convection and sea surface temperature. *J. Climate*, 5, 1140-1156.
- Myers, T. A., Mechoso, C. R., Cesana, G. V., DeFlorio, M. J., & Waliser, D. E. (2018). Cloud feedback key to marine heatwave off baja california. *Geophys. Res. Lett.*, 45(9), 4345-4352. Retrieved from <https://agupubs.onlinelibrary.wiley.com/doi/abs/10.1029/2018GL078242> doi: <https://doi.org/10.1029/2018GL078242>
- Nam, C., Bony, S., Dufresne, J.-L., & Chepfer, H. (2012). The 'too few, too bright' tropical low-cloud problem in cmip5 models. *Geophysical Research Letters*, 39(21). Retrieved from <https://agupubs.onlinelibrary.wiley.com/doi/abs/10.1029/2012GL053421> doi: <https://doi.org/10.1029/2012GL053421>
- Nigam, S. (1997). The annual warm to cold phase transition in the eastern equatorial pacific: Diagnosis of the role of stratus cloud-top cooling. *Journal of Climate*, 10(10), 2447 - 2467. Retrieved from [https://journals.ametsoc.org/view/journals/clim/10/10/1520-0442\\_1997\\_010\\_2447\\_tawtcp\\_2.0.co.2.xml](https://journals.ametsoc.org/view/journals/clim/10/10/1520-0442_1997_010_2447_tawtcp_2.0.co.2.xml) doi: [https://doi.org/10.1175/1520-0442\(1997\)010<2447:TAWTCP>2.0.CO;2](https://doi.org/10.1175/1520-0442(1997)010<2447:TAWTCP>2.0.CO;2)
- Philander, S. G. H., Gu, D., Lambert, G., Li, T., Halpern, D., Lau, N.-C., & Pacanowski, R. C. (1996). Why the ITCZ is mostly north of the equator. *J. Climate*, 9, 2958-2972. Retrieved from [http://dx.doi.org/10.1175/1520-0442\(1996\)009<2958:WTIIMN>2.0.CO;2](http://dx.doi.org/10.1175/1520-0442(1996)009<2958:WTIIMN>2.0.CO;2)
- Powell, M. D., Vickery, P. J., & Reinhold, T. A. (2003). Reduced drag coefficient for high wind speeds in tropical cyclones. *Nature*, 422, 279-283. doi: 10.1038/nature01481
- Raymond, D. J., Bretherton, C. S., & Molinari, J. (2006). Dynamics of the intertropical convergence zone of the east Pacific. *J. Atmos. Sci.*, 63, 582-597. doi: 10.1175/JAS3642.1
- Raymond, D. J., Esbensen, S. K., Paulson, C., Gregg, M., Bretherton, C. S., Petersen, W. A., ... Zuidema, P. (2004). Epic2001 and the coupled ocean-atmosphere system of the tropical east pacific. *Bull. Amer. Meteor. Soc.*, 85(9), 1341 - 1354. Retrieved from <https://journals.ametsoc.org/view/journals/bams/85/9/bams-85-9-1341.xml> doi: <https://doi.org/10.1175/BAMS-85-9-1341>



- Raymond, D. J., & Fuchs-Stone, v. (2021). Emergent Properties of Convection in OTREC and PREDICT. *J. Geophys. Res. Atmos.*, 126(4), e2020JD033585. doi: <https://doi.org/10.1029/2020JD033585>
- Schneider, T. (2017). Feedback of atmosphere-ocean coupling on shifts of the intertropical convergence zone. *Geophys. Res. Lett.*, 44(22), 11644–11653. doi: 10.1002/2017GL075817
- Schneider, T., Bischoff, T., & Haug, G. H. (2014). Migrations and dynamics of the intertropical convergence zone. *Nature*, 513, 45–53. doi: 10.1038/nature13636
- Schubert, W. H., Ciesielski, P. E., Lu, C., & Johnson, R. H. (1995). Dynamical adjustment of the trade wind inversion layer. *Journal of Atmospheric Sciences*, 52(16), 2941 - 2952. Retrieved from [https://journals.ametsoc.org/view/journals/atsc/52/16/1520-0469\\_1995\\_052\\_2941\\_daottw\\_2\\_0\\_co\\_2.xml](https://journals.ametsoc.org/view/journals/atsc/52/16/1520-0469_1995_052_2941_daottw_2_0_co_2.xml) doi: 10.1175/1520-0469(1995)052<2941:DAOTTW>2.0.CO;2
- Serra, Y. L., Rutledge, S. A., Chudler, K., & Zhang, C. (2023). Rainfall and convection in era5 and merra-2 over the northern equatorial western pacific during piston. *Journal of Climate*, 36(3), 845 - 863. Retrieved from <https://journals.ametsoc.org/view/journals/clim/36/3/JCLI-D-22-0203.1.xml> doi: <https://doi.org/10.1175/JCLI-D-22-0203.1>
- Sobel, A. H., & Neelin, J. D. (2006). The boundary layer contribution to intertropical convergence zones in the quasi-equilibrium tropical circulation model framework. *Theor. Comput. Fluid Dyn.* doi: 10.1007/s00162-006-0033-y
- Song, F., & Zhang, G. J. (2016). Effects of southeastern pacific sea surface temperature on the double-itzc bias in near cesm1. *Journal of Climate*, 29(20), 7417 - 7433. Retrieved from <https://journals.ametsoc.org/view/journals/clim/29/20/jcli-d-15-0852.1.xml> doi: 10.1175/JCLI-D-15-0852.1
- Stevens, B., Brogniez, H., Kiemle, C., Lacour, J.-L., Crevoisier, C., & Kiliani, J. (2017). Structure and dynamical influence of water vapor in the lower tropical troposphere. *Surveys in Geophysics*, 38, 1371–1397. Retrieved from <https://doi.org/10.1007/s10712-017-9420-8> doi: 10.1007/s10712-017-9420-8
- Stevens, B., & Coauthors. (2021). Eurec<sup>4</sup>a. *Earth System Science Data*, 13(8), 4067–4119. Retrieved from <https://essd.copernicus.org/articles/13/4067/2021/> doi: 10.5194/essd-13-4067-2021
- Stevens, B., Duan, J., McWilliams, J. C., Münnich, M., & Neelin, J. D. (2002). Entrainment, Rayleigh friction, and boundary layer winds over the tropical Pacific. *J. Climate*, 15, 30–44. doi: 10.1175/1520-0442(2002)015<0030:ERFABL>2.0.CO;2
- Takahashi, K., & Battisti, D. S. (2007). Processes controlling the mean tropical pacific precipitation pattern. part i: The andes and the eastern pacific itcz. *Journal of Climate*, 20(14), 3434 - 3451. Retrieved from <https://journals.ametsoc.org/view/journals/clim/20/14/jcli4198.1.xml> doi: <https://doi.org/10.1175/JCLI4198.1>
- Tomas, R. A., Holton, J. R., & Webster, P. J. (1999). The influence of cross-equatorial pressure gradients on the location of near-equatorial convection. *Quart. J. Roy. Meteor. Soc.*, 125, 1107–1127. doi: 10.1002/qj.1999.49712555603
- Waliser, D. E., & Gautier, C. (1993). A satellite-derived climatology of the ITCZ. *J. Climate*, 6, 2162–2174. Retrieved from [https://doi.org/10.1175/1520-0442\(1993\)006<2162:ASDCOT>2.0.CO;2](https://doi.org/10.1175/1520-0442(1993)006<2162:ASDCOT>2.0.CO;2) doi: 10.1175/1520-0442(1993)006<2162:ASDCOT>2.0.CO;2
- Wallace, J. M., Mitchell, T. P., & Deser, C. (1989). The influence of sea-surface temperature on surface wind in the eastern equatorial pacific: Seasonal and interannual variability. *Journal of Climate*, 2(12), 1492 - 1499. Retrieved from [https://journals.ametsoc.org/view/journals/clim/2/12/1520-0442\\_1989\\_002\\_1492\\_tiosst\\_2\\_0\\_co\\_2.xml](https://journals.ametsoc.org/view/journals/clim/2/12/1520-0442_1989_002_1492_tiosst_2_0_co_2.xml) doi: 10.1175/1520-0442(1989)002<1492:TIOSST>2.0.CO;2

- Woelfle, M. D., Bretherton, C. S., Hannay, C., & Neale, R. (2019). Evolution of the double-ITCZ bias through CESM2 development. *J. Adv. Model. Earth Syst.*, *11*(7), 1873–1893. doi: 10.1029/2019MS001647
- Wood, R. (2012). Stratocumulus clouds. *Monthly Weather Review*, *140*(8), 2373–2423. Retrieved from <https://journals.ametsoc.org/view/journals/mwre/140/8/mwr-d-11-00121.1.xml> doi: 10.1175/MWR-D-11-00121.1
- Xiang, B., Zhao, M., Held, I. M., & Golaz, J.-C. (2017). Predicting the severity of spurious “double ITCZ” problem in CMIP5 coupled models from AMIP simulations. *Geophys. Res. Lett.*, *44*(3), 1520–1527. Retrieved from <https://agupubs.onlinelibrary.wiley.com/doi/abs/10.1002/2016GL071992> doi: 10.1002/2016GL071992
- Xiang, B., Zhao, M., Ming, Y., Yu, W., & Kang, S. M. (2018). Contrasting impacts of radiative forcing in the southern ocean versus southern tropics on itcz position and energy transport in one gfdl climate model. *Journal of Climate*, *31*(14), 5609–5628. Retrieved from <https://journals.ametsoc.org/view/journals/clim/31/14/jcli-d-17-0566.1.xml> doi: 10.1175/JCLI-D-17-0566.1
- Xie, R., & Yang, Y. (2014). Revisiting the latitude fluctuations of the eastern pacific itcz during the central pacific el niño. *Geophys. Res. Lett.*, *41*(22), 7770–7776. Retrieved from <https://agupubs.onlinelibrary.wiley.com/doi/abs/10.1002/2014GL061857> doi: <https://doi.org/10.1002/2014GL061857>
- Xie, S.-P., Peng, Q., Kamae, Y., Zheng, X.-T., Tokinaga, H., & Wang, D. (2018). Eastern pacific itcz dipole and enso diversity. *Journal of Climate*, *31*(11), 4449–4462. Retrieved from <https://journals.ametsoc.org/view/journals/clim/31/11/jcli-d-17-0905.1.xml> doi: 10.1175/JCLI-D-17-0905.1
- Xie, S.-P., & Philander, S. G. H. (1994). A coupled ocean-atmosphere model of relevance to the itcz in the eastern pacific. *Tellus A: Dynamic Meteorology and Oceanography*, *46*(4), 340–350. Retrieved from <https://doi.org/10.3402/tellusa.v46i4.15484> doi: 10.3402/tellusa.v46i4.15484
- Yang, W., & Magnusdottir, G. (2016). Interannual signature in daily itcz states in the east pacific in boreal spring. *Journal of Climate*, *29*(22), 8013–8025. doi: 10.1175/JCLI-D-16-0395.1
- Yu, S., & Pritchard, M. S. (2019). A strong role for the AMOC in partitioning global energy transport and shifting ITCZ position in response to latitudinally discrete solar forcing in CESM1.2. *J. Climate*, *32*(8), 2207–2226. doi: 10.1175/JCLI-D-18-0360.1
- Zhang, C. (2001). Double ITCZs. *J. Geophys. Res.*, *106*, 11785–11792. doi: 10.1029/2001JD900046
- Zhang, G. J., Song, X., & Wang, Y. (2019). The double itcz syndrome in gcms: A coupled feedback problem among convection, clouds, atmospheric and ocean circulations. *Atmospheric Research*, *229*, 255–268. Retrieved from <https://www.sciencedirect.com/science/article/pii/S0169809518316788> doi: <https://doi.org/10.1016/j.atmosres.2019.06.023>
- Zhang, M. H., Lin, W. Y., Klein, S. A., Bacmeister, J. T., Bony, S., Cederwall, R. T., ... Zhang, J. H. (2005). Comparing clouds and their seasonal variations in 10 atmospheric general circulation models with satellite measurements. *Journal of Geophysical Research: Atmospheres*, *110*(D15). Retrieved from <https://agupubs.onlinelibrary.wiley.com/doi/abs/10.1029/2004JD005021> doi: <https://doi.org/10.1029/2004JD005021>
- Zhou, S., Huang, G., & Huang, P. (2020). Excessive itcz but negative sst biases in the tropical pacific simulated by cmip5/6 models: The role of the meridional pattern of sst bias. *Journal of Climate*, *33*(12), 5305–5316. Retrieved from <https://journals.ametsoc.org/view/journals/clim/33/12/jcli-d-19-0922.1.xml> doi: 10.1175/JCLI-D-19-0922.1